Precipitation over a wide range of climates simulated with comprehensive GCMs

David Bonan[1], Tapio Schneider[1], and Jiang Zhu[2]

[1]California Institute of Technology
[2]National Center for Atmospheric Research

April 25, 2024

Abstract

Idealized general circulation models (GCMs) suggest global-mean precipitation ceases to increase with warming in hot climates. However, it is unclear if this occurs in more comprehensive GCMs. Here, we examine precipitation over a wide range of climates simulated with comprehensive GCMs. We find that in the Community Atmosphere Model, global-mean precipitation increases approximately linearly with global-mean surface temperatures up to about 330˜K, where it peaks at 5˜mm˜day$ˆ{-1}$. Beyond 330˜K, global-mean precipitation decreases substantially despite increasing surface temperatures. This occurs because of increased atmospheric shortwave absorption from water vapor, which limits shortwave radiation available for surface evaporation. Precipitation decreases in the tropics and subtropics, but continues to increase in the extratropics due to increased poleward moisture transport. Precipitable water increases everywhere, resulting in longer water-vapor residence times and implying more episodic precipitation. Other GCMs indicate global-mean precipitation might exhibit a smaller maximum rate and begin to decrease at lower surface temperatures.

Precipitation over a wide range of climates simulated with comprehensive GCMs

David B. Bonan[1], **Tapio Schneider**[1], **Jiang Zhu**[2]

[1]Environmental Science and Engineering, California Institute of Technology, Pasadena, CA, USA
[2]Climate and Global Dynamics, NSF National Center for Atmospheric Research, Boulder, Colorado, USA

Key Points:

- Global-mean precipitation increases approximately linearly with surface temperatures up to 330 K, then decreases with higher temperatures
- Precipitation decreases at high temperatures due to increased atmospheric shortwave absorption from water vapor, limiting surface absorption
- At high temperatures, precipitation decreases in the tropics and subtropics, but increases in the extratropics due to moisture transport

Corresponding author: David B. Bonan, dbonan@caltech.edu

Abstract

Idealized general circulation models (GCMs) suggest global-mean precipitation ceases to increase with warming in hot climates. However, it is unclear if this occurs in more comprehensive GCMs. Here, we examine precipitation over a wide range of climates simulated with comprehensive GCMs. We find that in the Community Atmosphere Model, global-mean precipitation increases approximately linearly with global-mean surface temperatures up to about 330 K, where it peaks at 5 mm day^{-1}. Beyond 330 K, global-mean precipitation decreases substantially despite increasing surface temperatures. This occurs because of increased atmospheric shortwave absorption from water vapor, which limits shortwave radiation available for surface evaporation. Precipitation decreases in the tropics and subtropics, but continues to increase in the extratropics due to increased poleward moisture transport. Precipitable water increases everywhere, resulting in longer water-vapor residence times and implying more episodic precipitation. Other GCMs indicate global-mean precipitation might exhibit a smaller maximum rate and begin to decrease at lower surface temperatures.

Plain Language Summary

Earth's climate has experienced substantial changes over its history, including periods of extremely cold temperatures where most regions contained ice, and periods of extremely warm temperatures where most regions contained no ice. In this study, we explore how precipitation changed in extremely cold and warm climates using a unique set of coupled climate model simulations. We find that global-mean precipitation increases linearly with global-mean surface temperatures up to 330 K, where it peaks and then decreases as surface temperatures further increase. This occurs because in hot climates, global-mean precipitation is almost entirely balanced by absorbed shortwave radiation at the surface. As the climate warms, the atmosphere contains more water vapor, resulting in increased absorption of shortwave radiation within the atmosphere and decreased absorption of shortwave radiation at the surface. This limits the energy available for surface evaporation. We show that other climate models exhibit qualitatively similar behavior but indicate the peak in global-mean precipitation could occur at lower surface temperatures. These results demonstrate the need to better understand Earth's hydrological cycle in hot climates. These results also have large implications for understanding weathering in past climates and the habitability of other Earth-like planets.

1 Introduction

Global-mean precipitation is expected to increase at a rate of 1–3 % per degree of warming in response to rising greenhouse-gas concentrations (Allen & Ingram, 2002; Held & Soden, 2006; Vecchi & Soden, 2007; Jeevanjee & Romps, 2018). This relationship, often referred to as Earth's global hydrological sensitivity, has been found to be remarkably similar across a variety of greenhouse-gas forcing experiments (Stephens & Ellis, 2008; Lambert & Webb, 2008; Andrews & Forster, 2010; Andrews et al., 2010; O'Gorman et al., 2012; Pendergrass & Hartmann, 2014; DeAngelis et al., 2015; Fläschner et al., 2016; Raiter et al., 2023). This implies that global-mean precipitation in past climates, such as the early Eocene or the mid-Pliocene, can be inferred directly from paleoclimate temperature records. For example, it is estimated that early Eocene surface temperatures were 12–15 K warmer than the present-day climate (Caballero & Huber, 2013; Anagnostou et al., 2016; Inglis et al., 2020), which suggests that global-mean precipitation would have been 12–45 % larger than today.

While the global hydrological sensitivity is a conceptually convenient metric, there is evidence that it varies as a function of climate state, implying that estimates from climates similar to today may not apply to past climates. For instance, O'Gorman and Schneider (2008) simulated a wide range of climates in an idealized GCM and showed that global-mean precipitation ceases to increase with warming in hot climates. Examination of the surface energy budget showed that in hot climates, global-mean precipitation is entirely balanced by absorbed shortwave radiation at the surface, which in the idealized GCM, is insensitive to warming (O'Gorman & Schneider, 2008). However, the idealized GCM simulations employed a simple gray radiation scheme and contained no land, sea ice, or clouds, leaving questions about the behavior of precipitation in comprehensive GCMs.

More recent work examined precipitation in comprehensive GCMs under various atmospheric carbon dioxide (CO_2) levels and found that the global hydrological sensitivity exhibits weak climate state dependence. Good et al. (2012) used a coupled GCM and found that global-mean precipitation is only slightly less sensitive to warming in warm climates. Raiter et al. (2023) examined a broader suite of coupled GCMs and found that the global hydrological sensitivity changes little under large CO_2 forcing. However, these studies did not explore extremely high atmospheric CO_2 concentrations and only simulated a narrow range of Cenozoic Era surface temperatures. Thus, in comprehensive GCMs, it remains unclear whether the global hydrological sensitivity is weaker in hot climates and whether precipitation exhibits significant climate state dependence. Notably, analytical radiative arguments introduced by Jeevanjee and Romps (2018) suggest that in hot climates, precipitation may decrease under warming. Yet, this hypothesis has not been confirmed in comprehensive GCMs, which contain clouds and other processes that can modulate radiative fluxes.

In this study, we examine precipitation over a wide range of climates simulated with comprehensive GCMs. We find that in the Community Atmosphere Model (CAM), global-mean precipitation increases approximately linearly with global-mean surface temperatures up to about 330 K, where it peaks at a rate of approximately 5 mm day^{-1}. Beyond 330 K, global-mean precipitation decreases substantially despite increasing global-mean surface temperatures. The decrease in precipitation occurs because in hot climates, Earth's atmosphere contains more water vapor, resulting in increased absorption of shortwave radiation within the atmosphere and decreased absorption of shortwave radiation at the surface, thereby limiting the energy available for surface evaporation. Other GCMs indicate global-mean precipitation might exhibit a smaller maximum rate and begin to decrease at lower surface temperatures. We also find that extratropical precipitation continues to increase despite decreasing global-mean precipitation because of increased poleward latent energy transport. These results have large implications for understanding Earth's hydrological cycle across various epochs, spanning from the recent past to the Hadean and Archaean eons, as well as for understanding weathering in past climates, and the habitability of other Earth-like planets.

2 Data and methods

2.1 Climate model output

We use simulation output from a suite of comprehensive GCMs that have participated in different phases of the Coupled Model Intercomparison Project. The simulations come from different GCMs and span a wide range of surface temperatures, enabling us to explore the impact of model physics on precipitation as a function of climate state.

2.1.1 Community Atmosphere Model (CAM)

We use a suite of simulations from CAM4, CAM5, and CAM6, which are state-of-the-art atmospheric models within the Community Earth System Model (CESM; Hurrell et al., 2013; Danabasoglu et al., 2020). CAM4 uses different radiative transfer code (Collins et al., 2006) from CAM5 and CAM6, which both use the rapid radiative transfer model for GCMs (Mlawer et al., 1997). CAM4, CAM5, and CAM6 also differ substantially in their physical parameterizations of convection and clouds, leading to different equilibrium climate sensitivities of 3.1 K, 4.2 K, and 5.3 K, respectively (Zhu & Poulsen, 2020).

Each CAM simulation is performed with a slab-ocean model (SOM) and specified atmospheric CO_2 concentration. The framework is described in more detail by Zhu and Poulsen (2020). In short, CAM6 simulations were carried out with 1×, 2×, and 4× the preindusitrial CO_2 concentration (284.7 ppmv); CAM5 simulations were carried out with 1×, 2×, 4×, and 8× CO_2; and CAM4 simulations were carried out with 1×, 2×, 4×, 8×, 16×, 32× and 64× CO_2. With CAM4, we perform two additional simulations (128× and 256× CO_2) not described by Zhu and Poulsen (2020). Note that model instability for CAM6 with 8×CO_2 and CAM5 with 16×CO_2 prevented higher CO_2 simulations. Each set of SOM simulations employ identical non-CO_2 preindustrial boundary conditions and mixed layer depths and heat transport convergence derived from corresponding fully coupled preindustrial simulations with a dynamical ocean. All CAM4 and CAM5 simulations were run with a horizontal resolution of 1.9° × 2.5° (latitude × longitude) for 60 model years, except for the CAM4 64×, 128×, and 256×CO_2 simulations, which were run for 80 model years. All CAM6 simulations were run for 80 model years. The last 20 years of each simulation were used to calculate climatologies. The global-mean surface temperature range covered by these simulations is broadly comparable to paleoclimate temperatures over the Cenozoic Era and beyond.

We also use a suite of climate simulations that are described in more detail by Wolf et al. (2018). These simulations use a modified version of CAM4 with a SOM and a horizontal resolution of 4° × 5°. The modified version of CAM4 uses a correlated-k radiative transfer model to accurately simulate extremely warm climates (Wolf & Toon, 2013). We use 22 simulations with atmospheric CO_2 concentrations starting from 1.40625 ppmv and doubling until 2,949,120 ppmv.

2.1.2 LongRunMIP

We use a set of simulations from LongRunMIP (Rugenstein et al., 2019), which is a model intercomparison project that aims to better understand centennial and millennial time scale atmosphere–ocean processes in comprehensive, coupled GCMs. We use all GCMs that provide a preindustrial control simulation and 2×, 4×, 8×, and 16× CO_2. There are no simulations with higher CO_2 forcing. We assume that each preindustrial control simulation has an atmospheric CO_2 concentration of 284.7 ppmv. For all simulations, except those from CNRM-CM6-1, we average each variable over years 970–1,000. For the CNRM-CM6-1 simulations, we average over years 720–750 as this is the longest available time period after 2×CO_2. Most simulations have little-to-no global-mean ocean heat uptake and are therefore close to equilibrium at this time period.

2.2 Energy budget diagnostics

2.2.1 Global

Global-mean precipitation can be examined through the surface energy budget. The global-mean (denoted by an overbar) surface energy budget can be expressed as

$$0 = \bar{S} - \bar{L} - L_v\bar{E} - \bar{H} - \bar{G}, \tag{1}$$

where S is the net downward shortwave flux, L is the net upward longwave flux, E is the surface evaporation flux, L_v is the latent heat of vaporization, H is the sensible heat flux from the surface into the atmosphere, and G is ocean heat uptake and storage. On interannual and longer timescales, $\bar{E}$ is equal to precipitation $\bar{P}$, which results in

$$\bar{P} \equiv \bar{E} = \frac{1}{L_v}\left(\bar{S} - \bar{L} - \bar{H} - \bar{G}\right). \tag{2}$$

The radiative fluxes S and L can be further decomposed into clear-sky (clr) and cloud components (cld) such that $S = S_{\mathrm{clr}} + S_{\mathrm{cld}}$ and $L = L_{\mathrm{clr}} + L_{\mathrm{cld}}$. For the CAM simulations, we decompose S and L into clear-sky and cloud components, while for the LongRunMIP simulations, we cannot decompose S and L due to the lack of clear-sky surface flux output.

O'Gorman and Schneider (2008) showed that Eq. (2) can explain the structure of global-mean precipitation as a function of climate state, including the processes controlling the maximum rate of precipitation in hot climates.

2.2.2 Regional

Regional precipitation can also be examined through the surface energy budget with the addition of the latent energy flux divergence $\nabla \cdot F_{\mathrm{latent}}$. On long time scales,

$$P - E = -\frac{1}{L_v}\nabla \cdot F_{\mathrm{latent}}, \tag{3}$$

which means that, using the surface energy budget, regional precipitation can be expressed as

$$P = \frac{1}{L_v}\left(S - L - H - G - \nabla \cdot F_{\mathrm{latent}}\right). \tag{4}$$

We examine regional precipitation through the surface energy budget as it connects directly to our approach for global-mean precipitation and provides a physically intuitive understanding of energetic constraints on evaporation, which is how moisture enters the atmosphere. Note that integrating Eq. (4) globally results in exactly Eq. (2). Global and regional precipitation can also be examined through the atmospheric energy budget (e.g., Muller & O'Gorman, 2011; O'Gorman et al., 2012; Pendergrass & Hartmann, 2014; Bonan, Feldl, et al., 2023).

3 Precipitation over a wide range of climates

3.1 Global-mean precipitation

We begin by examining global-mean precipitation as a function of atmospheric CO_2 concentration and global-mean surface temperature (Fig. 1). Under high CO_2 concentrations, GCMs exhibit large intermodel differences in global-mean surface temperatures (Fig. 1a). For example, across GCMs, global-mean surface temperatures for CO_2 concentrations near 1,000 ppmv range from 289 K to 300 K. While the intermodel spread in surface temperatures is large, these simulations, with the exception of CAM4 (blue and red lines, Fig. 1a), only span a small range of Cenezoic Era paleoclimate temperatures. The two versions of CAM4 with different radiation schemes simulate an even larger range of global-mean surface temperatures, ranging from 265 K to 380 K (blue and red lines, Fig. 1a). Note these simulations indicate that Earth's climate sensitivity exhibits considerable state dependence for global-mean surface temperatures around 310 K, which has been noted in several other studies (e.g., Caballero & Huber, 2013; Wolf et al., 2018; Zhu & Poulsen, 2020; Seeley & Jeevanjee, 2021; Henry et al., 2023).

GCMs also exhibit a large intermodel spread in global-mean precipitation as a function of atmospheric CO_2 concentration (Fig. 1b). For example, across GCMs, global-mean precipitation for CO_2 concentrations near 1,000 ppmv ranges from approximately 2.8 mm day^{-1} to approximately 4.0 mm day^{-1}. Interestingly, for CO_2 concentrations beyond 30,000 ppmv, the CAM4 simulations indicate that global-mean precipitation decreases (Fig. 1b) despite surface temperature increases (Fig. 1a). Both versions of CAM4 exhibit a global-mean precipitation decrease, despite having different radiation codes (blue and red lines, Fig. 1b).

These results can be further understood by plotting global-mean precipitation as a function of global-mean surface temperature; the derivative of this function is the global hydrological sensitivity (Fig. 1c). From cold (~ 270 K) to warm (~ 320 K) climates, global-mean precipitation exhibits a fairly linear relationship with global-mean surface temperature, with only slight decreases in the rate of global-mean precipitation increase. In hot (> 320 K) climates, the CAM4 simulations indicate that global-mean precipitation increases more slowly with global-mean surface temperature and eventually decreases at approximately 330 K (Fig. 1c). In the CAM4 simulation with the more accurate radiation code, global-mean precipitation continues to decrease substantially despite increasing surface temperatures. Note that other GCMs, such as MPI-ESM1.2 and HadCM3L, exhibit overall weaker increases in precipitation for the same surface temperature range as the CAM simulations (gold and light blue lines, Fig. 1c).

To understand the mechanisms contributing to global-mean precipitation as a function of global-mean surface temperature, we examine the surface energy budget (see Section 2.2.1). Figure 2 shows the components of the surface energy budget (converted from W m^{-2} to mm day^{-1}). The clear-sky and cloud components of the net surface shortwave and net surface longwave fluxes are shown in Figure S1.

From cold to warm climates, the global-mean net surface shortwave flux exhibits relatively little change, though there is large intermodel spread (Fig. 2a). For example, the CAM simulations exhibit little change in the net surface shortwave flux, whereas MPI-ESM1.2 exhibits a strong decrease. From cold to warm climates, both the net surface longwave flux and surface sensible heat flux approach zero with little intermodel spread (Fig. 2b and 2c). The net surface longwave flux change is almost entirely driven by the clear-sky component (Fig. S1).

In hot climates, the net surface longwave flux and surface sensible heat flux are zero or slightly positive (Fig. 2b, 2c). This occurs because differences in surface and tropospheric air temperatures become small, and the atmosphere approaches the optically thick limit, where upward longwave emission at the surface and the downward longwave emission from within the atmosphere that reaches the surface occur at almost the same temperature (O'Gorman & Schneider, 2008). As a result, global-mean evaporation, and thus global-mean precipitation, is almost entirely balanced by the net surface shortwave flux, which exhibits a strong decrease in hot climates (Fig. 2a). The clear-sky component of the net surface shortwave flux decreases in hot climates (Fig. S1) because of increased shortwave absorption by the atmosphere due to water vapor (Fig. S2). The decrease in net surface shortwave flux occurs in both CAM4 simulations, though the decrease is stronger at high temperatures in the CAM4 simulations with the more accurate radiation code (blue and red lines, Fig. 2a).

3.2 Zonal-mean precipitation

We now examine zonal-mean precipitation as a function of global-mean surface temperature (Fig. 3). We focus on the CAM simulations to understand the regions contributing to the decrease in global-mean precipitation for surface temperatures beyond 330 K. The same analysis for each simulation from LongRunMIP is shown in Figure S3.

From cold to warm climates, precipitation increases in most regions, with substantial increases in the tropics and extratropics and small decreases in the subtropics (Fig. 3a). In hot climates (> 320 K), subtropical and tropical precipitation decreases substantially. The maximum tropical precipitation is approximately 10 mm day^{-1} in warm climates and decreases to approximately 5 mm day^{-1} in hot climates. Similarly, subtropical precipitation decreases from approximately 6 mm day^{-1} in warm climates to approximately 0 mm day^{-1} in hot climates. Notably, from warm to hot climates, despite a decrease in global-mean precipitation, precipitation continues to increase in the extratropics, with the polar regions experiencing a substantial increase in precipitation (Fig. 3a). Precipitation in the Arctic, for instance, increases from approximately 2 mm day^{-1} in warm climates to approximately 8 mm day^{-1} in hot climates.

To understand the mechanisms contributing to regional precipitation as a function of global-mean surface temperature, we examine components of the surface energy budget and latent energy flux divergence (see Section 2.2.2). Figures 3b-e show the components of the zonal-mean surface energy budget and latent energy flux divergence (converted from W m^{-2} to mm day^{-1}) for the CAM simulations.

From cold to warm climates, the net surface shortwave flux remains relatively constant, exhibiting weak increases in the polar regions (Fig. 3b). Figure S4 shows the clear-sky and cloud components of the zonal-mean net surface shortwave flux and shows that this is related mainly to the clear-sky component. The overall increase in zonal-mean precipitation from cold to warm climates is contributed mainly by the net surface longwave flux, which becomes smaller under warming (Fig. 3c). The surface sensible heat flux contributes weakly to the overall increase in zonal-mean precipitation from cold to warm climates (Fig. 3d). The latent energy flux divergence contributes most to the zonal-mean pattern of precipitation, causing a precipitation increase in the tropics and extratropics, and a precipitation decrease in the subtropics (Fig. 3e). Note there are substantial changes in the latent energy flux divergence around 320 K that indicate meridional shifts in tropical rainfall, expansion of the subtropics, and poleward shifts of the midlatitude stormtracks.

In hot climates (> 320 K), the net surface longwave flux and surface sensible heat flux become much smaller and approach zero (Fig. 3c, 3d). As a result, in hot climates, regional precipitation is almost entirely balanced by the net surface shortwave flux and latent energy flux divergence (Fig. 3b, 3e). In the subtropics, the weak export of moisture associated with increased poleward latent energy transport (Fig. 3e) is balanced almost entirely by the net surface shortwave flux, resulting in no precipitation (Fig. 3a). Note that the subtropics continue to see drying in extremely hot climates, largely due to the increased latent energy transport (Fig. 3e). In the extratropics, precipitation continues to increase in hot climates because of increased poleward latent energy transport. In the polar regions, the decrease in net surface shortwave flux is small (Fig. 3b), but the increase in poleward latent energy transport is large (Fig. 3e), resulting in a overall precipitation increase (Fig. 3a).

3.3 Total precipitable water and precipitation intensity

The decrease in global-mean precipitation for surface temperatures above 330 K has important implications for precipitation intensity and precipitation extremes. Scaling arguments and simulations suggest that precipitation extremes depend primarily on the atmospheric water vapor content (O'Gorman & Schneider, 2009; O'Gorman & Schneider, 2009), which should continue to increase with warming (O'Gorman & Schneider, 2008). A decrease in global-mean precipitation but increase in global-mean atmospheric water vapor content implies that precipitation would have to become more episodic and potentially more intense.

Due to the lack of high-frequency temporal output, we are unable to quantitatively examine precipitation extremes (e.g., O'Gorman & Schneider, 2009; O'Gorman & Schneider, 2009). However, we can examine the total precipitable water and calculate the water vapor residence time, defined as the global-mean total precipitable water divided by the global-mean precipitation (Trenberth, 1998; Bosilovich et al., 2005). The water vapor residence time can help indicate precipitation intensity. For instance, a climate with the same mean precipitation as today but a longer water vapor residence time implies there is more episodic and intense precipitation.

The global-mean total precipitable water (Fig. 4a) and global-mean water vapor residence time (Fig. 4b) increase with increasing global-mean surface temperatures. From cold to warm climates, total precipitable water increases at a rate of 6–7 % K^{-1} and the water vapor residence time increases at a rate of 4–5 % K^{-1}. In hot climates, the total precipitable water continues to increase (Fig. 4a), resulting in a global-mean water vapor residence time of approximately one year at 350 K (Fig. 4b). The total precipitable water increases most in the tropics and subtropics (Fig. 4c), which likely results in regional variations of precipitation intensity. For climates between 320–330 K, precipitation is likely more intense and episodic due to the relatively similar global-mean precipitation (Fig. 1c) but increase in water vapor residence time (Fig. 4b).

4 Discussion and conclusions

In this study, we examined precipitation over a wide range of climates simulated with comprehensive GCMs. Building on earlier work by O'Gorman and Schneider (2008), we showed that global-mean precipitation increases approximately linearly with global-mean surface temperatures from cold to warm climates and begins to increase more slowly in hot climates (Fig. 1c)—consistent with Good et al. (2012). However, in contrast to these studies, we found that global-mean precipitation decreases substantially after 330 K, despite increasing surface temperatures (Fig. 1c). This occurs because global-mean precipitation is almost entirely balanced by the absorbed shortwave radiation at the surface in hot climates (Fig. 2). As the climate warms, Earth's atmosphere contains more water vapor, resulting in increased absorption of shortwave radiation within the atmosphere and decreased absorption of shortwave radiation at the surface (Fig. 2a and Fig. S2). This limits the energy available for surface evaporation and causes a decrease in global-mean precipitation with further warming. The results confirm the analytical radiative arguments of Jeevanjee and Romps (2018) but in comprehensive GCMs with cloud radiative processes.

The decrease in global-mean precipitation for surface temperatures beyond 330 K is driven by a decrease in tropical and subtropical precipitation (Fig. 3a). Extratropical precipitation continues to increase, despite a decrease in global-mean precipitation (Fig. 3a). This occurs because of increases in poleward latent energy transport (Fig. 3e), which is a well-known feature of hot climates (Caballero & Langen, 2005; O'Gorman & Schneider, 2008). However, the increase in poleward latent energy transport exhibits significant deviations from the increase expected solely from the Clausius-Clapeyron relation (Held & Soden, 2006). These deviations include meridional shifts in tropical rainfall, expansions and contractions of the subtropical regions, and poleward migrations of the extratropical storm tracks. A series of studies have shown that a one-dimensional moist energy balance model can accurately simulate poleward moisture transport in comprehensive GCMs (Siler et al., 2018; Armour et al., 2019; Bonan, Siler, et al., 2023; Bonan et al., 2024), suggesting that downgradient energy transport might explain the range of poleward latent transport seen in CAM4, including dynamical changes associated with the Hadley circulations.

While our results show considerable climate state dependence in precipitation, the simulations used are driven purely by changes in atmospheric CO_2 concentrations and do not contain changes in other boundary conditions that impact hot climates (see review by Zhu et al., 2024). For example, the early Eocene experienced significant changes in orbital dynamics (Lourens et al., 2005) as well as in continental land configurations and ocean circulation (Barron, 1987; Shellito et al., 2009; Green & Huber, 2013), each of which could potentially alter the surface energy budget. Examining the effect of other forcings on precipitation in hot climates might change these results.

Despite this caveat, our work has implications for other aspects of Earth's hydrological cycle. We showed that global-mean total precipitable water increases more strongly with warming when compared to global-mean precipitation (Fig. 4a and Fig. 1c), which results in a longer global-mean water vapor residence time (Fig. 4b). Thus, precipitation would have to become more episodic at high surface temperatures. However, due to the lack of higher-frequency output we are unable to quantitatively examine precipitation intensity and precipitation extremes. Note that recent work showed precipitation in hot climates is indeed more episodic and occurs in short and intense outbursts separated by multi-day dry spells (Seeley & Wordsworth, 2021; Dagan et al., 2023). However, these studies employed an idealized cloud-resolving model with limited domains. It remains unclear what episodic precipitation looks like in hot climates simulated with comprehensive GCMs. Future work should explore other characteristics of precipitation in hot climates. Such work will help to better understand mechanisms for hydrological change in past and future climates.

Overall, our results show that precipitation is strongly dependent on the climate state. While the CAM simulations indicate that global-mean precipitation exhibits a maximum rate of approximately 5 mm day^{-1} and decreasing rates for surface temperatures beyond 330 K, other GCMs, like HadCM3L and MPI-ESM1.2, indicate that global-mean precipitation might exhibit a smaller maximum rate and begin to decrease at lower surface temperatures. These differences are attributable to shortwave radiation and may be related to water vapor absorption parameterizations in comprehensive GCMs (e.g., Yang et al., 2016). Hence, there is a need to examine Earth's hydrological cycle in hot climates simulated with a broader suite of comprehensive GCMs. Such work will have large implications for understanding various climate epochs, spanning from the recent past to the Hadean and Archaean eons, as well as for understanding weathering in past climates, and the habitability of other Earth-like planets.

Acknowledgments

The authors thank Thorsten Mauritsen for helpful comments during early stages of this research. D.B.B was supported the National Science Foundation (NSF) Graduate Research Fellowship Program (NSF Grant DGE1745301). This material is based upon work supported by the National Center for Atmospheric Research (NCAR), which is a major facility sponsored by the NSF under Cooperative Agreement 1852977.

Data Availability Statement

CAM4, CAM5, and CAM6 output is available in the Zenodo repository (`https://doi.org/10.5281/zenodo.3695929`). LongRunMIP output is freely available at `http://www.longrunmip.org/`. The CAM4 output with modified radiation is available at: `https://archive.org/download/EvaluatingClimateSensitivityToCO2AcrossEarthsHistory_201809`

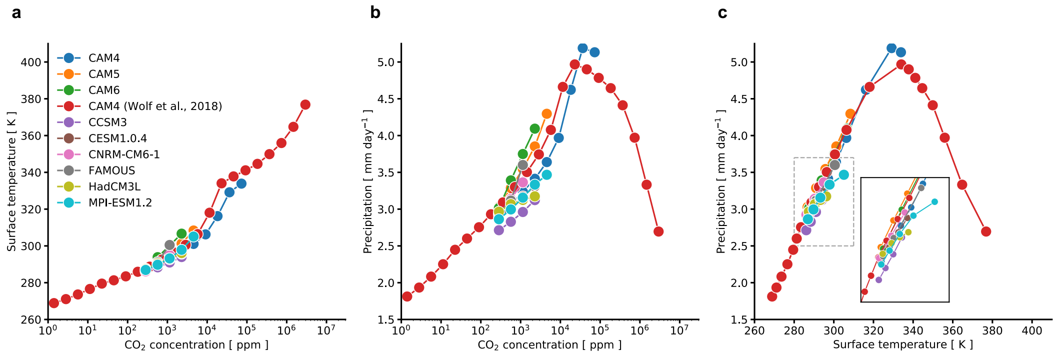

Figure 1. Global-mean precipitation over a wide range of climates. (a) Global-mean surface temperature (K) as a function of the atmospheric CO_2 concentration for the CAM slab-ocean model simulations and fully-coupled LongRunMIP simulations. (b) Same as in (a) but for global-mean precipitation (mm day^{-1}). (c) Same as in (b) but for global-mean precipitation as a function of global-mean surface temperature. The inset in (c) shows an enlarged version of the grey dashed box.

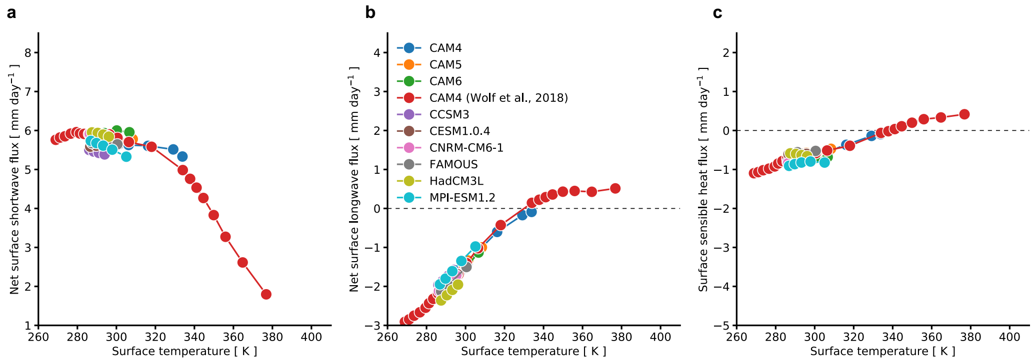

Figure 2. Contributions to global-mean precipitation over a wide range of climates. The global-mean (a) net surface shortwave flux, (b) net surface longwave flux, and (c) surface sensible heat flux as a function of global-mean surface temperature for the CAM slab-ocean model simulations and fully-coupled LongRunMIP simulations. Ocean heat uptake is near-zero for all simulations and is not shown.

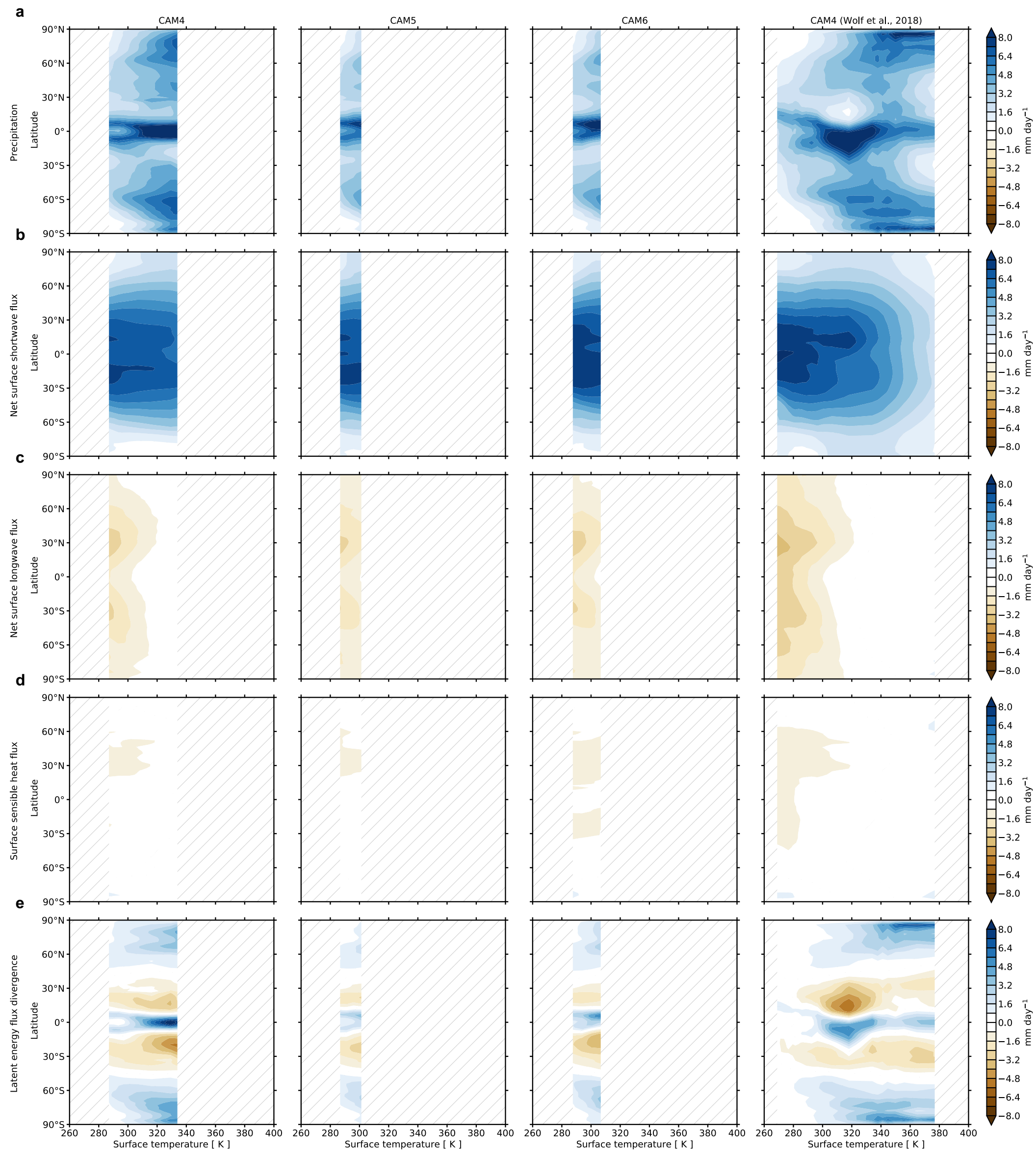

Figure 3. Zonal-mean precipitation over a wide range of climates. (a) The zonal-mean precipitation as a function of global-mean surface temperature for the CAM4, CAM5, and CAM6 simulations. The zonal-mean (b) net surface shortwave flux, (c) net surface longwave flux, (d) surface sensible heat flux, and (e) latent energy flux divergence (converted from W m^{-2} to mm day^{-1}) as a function of global-mean surface temperature for the CAM4, CAM5, and CAM6 simulations. Ocean heat uptake is zero for all simulations and is not shown. Panels (b-e) add to panel (a). The light grey hatching indicates no simulation data.

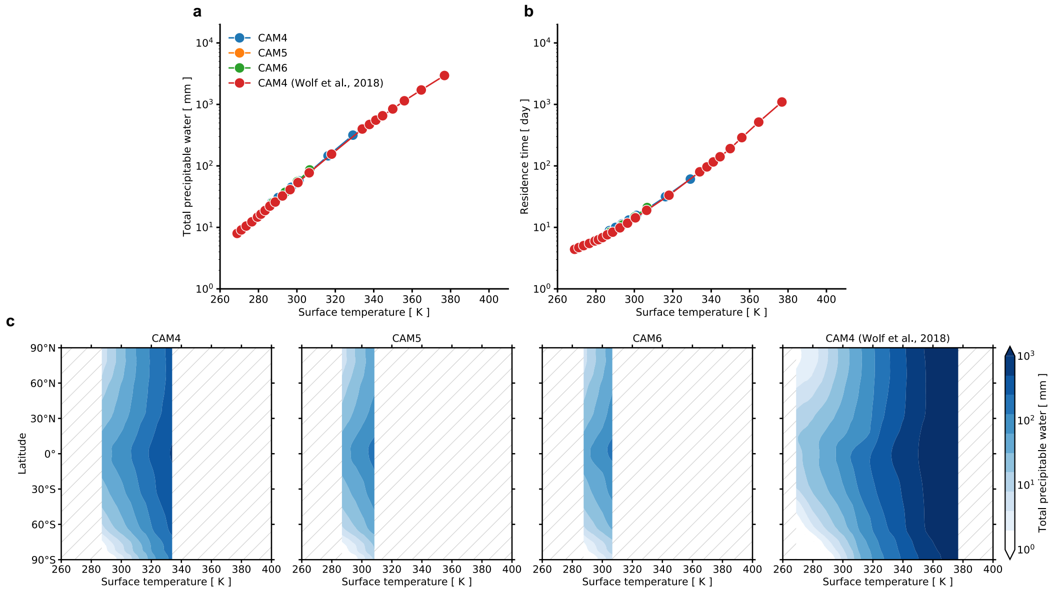

Figure 4. Residence time of water vapor over a wide range of climates. The global-mean (a) total precipitable water and (b) residence time of water vapor. The (blue) CAM4, (orange) CAM5, and (green) CAM6 simulations use a slab-ocean model with the Rapid Radiative Transfer Model and the (red) CAM4 simulation uses a slab-ocean model with a more accurate radiation model for high temperatures. (c) Zonal-mean total precipitable water as a function of global-mean surface temperature for the CAM4, CAM5, and CAM6 simulations. The light grey hatching indicates no simulation data.

References

Allen, M. R., & Ingram, W. J. (2002). Constraints on future changes in climate and the hydrologic cycle. *Nature*, *419*(6903), 224–232.

Anagnostou, E., John, E. H., Edgar, K. M., Foster, G. L., Ridgwell, A., Inglis, G. N., ... Pearson, P. N. (2016). Changing atmospheric CO2 concentration was the primary driver of early Cenozoic climate. *Nature*, *533*(7603), 380–384.

Andrews, T., & Forster, P. M. (2010). The transient response of global-mean precipitation to increasing carbon dioxide levels. *Environmental Research Letters*, *5*(2), 025212.

Andrews, T., Forster, P. M., Boucher, O., Bellouin, N., & Jones, A. (2010). Precipitation, radiative forcing and global temperature change. *Geophysical research letters*, *37*(14).

Armour, K. C., Siler, N., Donohoe, A., & Roe, G. H. (2019). Meridional atmospheric heat transport constrained by energetics and mediated by large-scale diffusion. *Journal of Climate*, *32*(12), 3655–3680.

Barron, E. J. (1987). Eocene equator-to-pole surface ocean temperatures: A significant climate problem? *Paleoceanography*, *2*(6), 729–739.

Bonan, D. B., Feldl, N., Siler, N., Kay, J. E., Armour, K. C., Eisenman, I., & Roe, G. H. (2024). The influence of climate feedbacks on regional hydrological changes under global warming. *Geophysical Research Letters*, *51*(3), e2023GL106648.

Bonan, D. B., Feldl, N., Zelinka, M. D., & Hahn, L. C. (2023). Contributions to regional precipitation change and its polar-amplified pattern under warming. *Environmental Research: Climate*, *2*(3), 035010.

Bonan, D. B., Siler, N., Roe, G. H., & Armour, K. C. (2023). Energetic constraints on the pattern of changes to the hydrological cycle under global warming. *Journal of Climate*, *36*(10), 3499–3522.

Bosilovich, M. G., Schubert, S. D., & Walker, G. K. (2005). Global changes of the water cycle intensity. *Journal of Climate*, *18*(10), 1591–1608.

Caballero, R., & Huber, M. (2013). State-dependent climate sensitivity in past warm climates and its implications for future climate projections. *Proceedings of the National Academy of Sciences*, *110*(35), 14162–14167.

Caballero, R., & Langen, P. L. (2005). The dynamic range of poleward energy transport in an atmospheric general circulation model. *Geophysical Research Letters*, *32*(2).

Collins, W. D., Bitz, C. M., Blackmon, M. L., Bonan, G. B., Bretherton, C. S., Carton, J. A., ... others (2006). The community climate system model version 3 (CCSM3). *Journal of Climate*, *19*(11), 2122–2143.

Dagan, G., Seeley, J. T., & Steiger, N. (2023). Convection and Convective-Organization in Hothouse Climates. *Journal of Advances in Modeling Earth Systems*, *15*(11), e2023MS003765.

Danabasoglu, G., Lamarque, J.-F., Bacmeister, J., Bailey, D., DuVivier, A., Edwards, J., ... others (2020). The community earth system model version 2 (CESM2). *Journal of Advances in Modeling Earth Systems*, *12*(2), e2019MS001916.

DeAngelis, A. M., Qu, X., Zelinka, M. D., & Hall, A. (2015). An observational radiative constraint on hydrologic cycle intensification. *Nature*, *528*(7581), 249–253.

Fläschner, D., Mauritsen, T., & Stevens, B. (2016). Understanding the intermodel spread in global-mean hydrological sensitivity. *Journal of Climate*, *29*(2), 801–817.

Good, P., Ingram, W., Lambert, F. H., Lowe, J. A., Gregory, J. M., Webb, M. J., ... Wu, P. (2012). A step-response approach for predicting and understanding non-linear precipitation changes. *Climate Dynamics*, *39*, 2789–2803.

Green, J., & Huber, M. (2013). Tidal dissipation in the early Eocene and implications for ocean mixing. *Geophysical Research Letters*, *40*(11), 2707–2713.

Held, I. M., & Soden, B. J. (2006). Robust responses of the hydrological cycle to global warming. *Journal of climate*, *19*(21), 5686–5699.

Henry, M., Vallis, G. K., Lutsko, N. J., Seeley, J. T., & McKim, B. A. (2023). State-Dependence of the Equilibrium Climate Sensitivity in a Clear-Sky GCM. *Geophysical Research Letters*, *50*(23), e2023GL104413.

Hurrell, J. W., Holland, M. M., Gent, P. R., Ghan, S., Kay, J. E., Kushner, P. J., ... others (2013). The community earth system model: a framework for collaborative research. *Bulletin of the American Meteorological Society*, *94*(9), 1339–1360.

Inglis, G. N., Bragg, F., Burls, N., Evans, D., Foster, G. L., Huber, M., ... others (2020). Global mean surface temperature and climate sensitivity of the EECO, PETM and latest Paleocene. *Climate of the past Discussions*, *2020*, 1–43.

Jeevanjee, N., & Romps, D. M. (2018). Mean precipitation change from a deepening troposphere. *Proceedings of the National Academy of Sciences*, *115*(45), 11465–11470.

Lambert, F. H., & Webb, M. J. (2008). Dependency of global mean precipitation on surface temperature. *Geophysical Research Letters*, *35*(16).

Lourens, L. J., Sluijs, A., Kroon, D., Zachos, J. C., Thomas, E., Röhl, U., ... Raffi, I. (2005). Astronomical pacing of late Palaeocene to early Eocene global warming events. *Nature*, *435*(7045), 1083–1087.

Mlawer, E. J., Taubman, S. J., Brown, P. D., Iacono, M. J., & Clough, S. A. (1997). Radiative transfer for inhomogeneous atmospheres: RRTM, a validated correlated-k model for the longwave. *Journal of Geophysical Research: Atmospheres*, *102*(D14), 16663–16682.

Muller, C. J., & O'Gorman, P. (2011). An energetic perspective on the regional response of precipitation to climate change. *Nature Climate Change*, *1*(5), 266–271.

O'Gorman, P. A., & Schneider, T. (2009). The physical basis for increases in precipitation extremes in simulations of 21st-century climate change. *Proceedings of the National Academy of Sciences*, *106*(35), 14773–14777.

O'Gorman, P. A., Allan, R. P., Byrne, M. P., & Previdi, M. (2012). Energetic constraints on precipitation under climate change. *Surveys in geophysics*, *33*, 585–608.

O'Gorman, P. A., & Schneider, T. (2008). The hydrological cycle over a wide range of climates simulated with an idealized GCM. *Journal of Climate*, *21*(15), 3815–3832.

O'Gorman, P. A., & Schneider, T. (2009). Scaling of precipitation extremes over a wide range of climates simulated with an idealized GCM. *Journal of Climate*, *22*(21), 5676–5685.

Pendergrass, A. G., & Hartmann, D. L. (2014). The atmospheric energy constraint on global-mean precipitation change. *Journal of climate*, *27*(2), 757–768.

Raiter, D., Polvani, L. M., Mitevski, I., Pendergrass, A. G., & Orbe, C. (2023). Little change in apparent hydrological sensitivity at large CO2 forcing. *Geophysical Research Letters*, *50*(18), e2023GL104954.

Rugenstein, M., Bloch-Johnson, J., Abe-Ouchi, A., Andrews, T., Beyerle, U., Cao, L., ... others (2019). LongRunMIP: motivation and design for a large collection of millennial-length AOGCM simulations. *Bulletin of the American Meteorological Society*, *100*(12), 2551–2570.

Seeley, J. T., & Jeevanjee, N. (2021). H2O windows and CO2 radiator fins: A clear-sky explanation for the peak in equilibrium climate sensitivity. *Geophysical Research Letters*, *48*(4), e2020GL089609.

Seeley, J. T., & Wordsworth, R. D. (2021). Episodic deluges in simulated hothouse climates. *Nature*, *599*(7883), 74–79.

Shellito, C. J., Lamarque, J.-F., & Sloan, L. C. (2009). Early Eocene Arctic climate sensitivity to pCO2 and basin geography. *Geophysical Research Letters*, *36*(9).

Siler, N., Roe, G. H., & Armour, K. C. (2018). Insights into the zonal-mean response of the hydrologic cycle to global warming from a diffusive energy balance model. *Journal of Climate*, *31*(18), 7481–7493.

Stephens, G. L., & Ellis, T. D. (2008). Controls of global-mean precipitation increases in global warming GCM experiments. *Journal of Climate*, *21*(23), 6141–6155.

Trenberth, K. E. (1998). Atmospheric moisture residence times and cycling: Implications for rainfall rates and climate change. *Climatic change*, *39*, 667–694.

Vecchi, G. A., & Soden, B. J. (2007). Global warming and the weakening of the tropical circulation. *Journal of Climate*, *20*(17), 4316–4340.

Wolf, E., Haqq-Misra, J., & Toon, O. (2018). Evaluating climate sensitivity to CO2 across Earth's history. *Journal of Geophysical Research: Atmospheres*, *123*(21), 11–861.

Wolf, E., & Toon, O. (2013). Hospitable Archean climates simulated by a general circulation model. *Astrobiology*, *13*(7), 656–673.

Yang, J., Leconte, J., Wolf, E. T., Goldblatt, C., Feldl, N., Merlis, T., ... others (2016). Differences in water vapor radiative transfer among 1D models can significantly affect the inner edge of the habitable zone. *The Astrophysical Journal*, *826*(2), 222.

Zhu, J., & Poulsen, C. J. (2020). On the increase of climate sensitivity and cloud feedback with warming in the community atmosphere models. *Geophysical Research Letters*, *47*(18), e2020GL089143.

Zhu, J., Poulsen, C. J., & Otto-Bliesner, B. L. (2024). Modeling Past Hothouse Climates as a Means for Assessing Earth System Models and Improving the Understanding of Warm Climates. *Annual Review of Earth and Planetary Sciences*, *52*.

Precipitation over a wide range of climates simulated with comprehensive GCMs

David B. Bonan[1], Tapio Schneider[1], Jiang Zhu[2]

[1]Environmental Science and Engineering, California Institute of Technology, Pasadena, CA, USA
[2]Climate and Global Dynamics, NSF National Center for Atmospheric Research, Boulder, Colorado, USA

Key Points:

- Global-mean precipitation increases approximately linearly with surface temperatures up to 330 K, then decreases with higher temperatures
- Precipitation decreases at high temperatures due to increased atmospheric shortwave absorption from water vapor, limiting surface absorption
- At high temperatures, precipitation decreases in the tropics and subtropics, but increases in the extratropics due to moisture transport

Corresponding author: David B. Bonan, `dbonan@caltech.edu`

Abstract

Idealized general circulation models (GCMs) suggest global-mean precipitation ceases to increase with warming in hot climates. However, it is unclear if this occurs in more comprehensive GCMs. Here, we examine precipitation over a wide range of climates simulated with comprehensive GCMs. We find that in the Community Atmosphere Model, global-mean precipitation increases approximately linearly with global-mean surface temperatures up to about 330 K, where it peaks at 5 mm day^{-1}. Beyond 330 K, global-mean precipitation decreases substantially despite increasing surface temperatures. This occurs because of increased atmospheric shortwave absorption from water vapor, which limits shortwave radiation available for surface evaporation. Precipitation decreases in the tropics and subtropics, but continues to increase in the extratropics due to increased poleward moisture transport. Precipitable water increases everywhere, resulting in longer water-vapor residence times and implying more episodic precipitation. Other GCMs indicate global-mean precipitation might exhibit a smaller maximum rate and begin to decrease at lower surface temperatures.

Plain Language Summary

Earth's climate has experienced substantial changes over its history, including periods of extremely cold temperatures where most regions contained ice, and periods of extremely warm temperatures where most regions contained no ice. In this study, we explore how precipitation changed in extremely cold and warm climates using a unique set of coupled climate model simulations. We find that global-mean precipitation increases linearly with global-mean surface temperatures up to 330 K, where it peaks and then decreases as surface temperatures further increase. This occurs because in hot climates, global-mean precipitation is almost entirely balanced by absorbed shortwave radiation at the surface. As the climate warms, the atmosphere contains more water vapor, resulting in increased absorption of shortwave radiation within the atmosphere and decreased absorption of shortwave radiation at the surface. This limits the energy available for surface evaporation. We show that other climate models exhibit qualitatively similar behavior but indicate the peak in global-mean precipitation could occur at lower surface temperatures. These results demonstrate the need to better understand Earth's hydrological cycle in hot climates. These results also have large implications for understanding weathering in past climates and the habitability of other Earth-like planets.

1 Introduction

Global-mean precipitation is expected to increase at a rate of 1–3 % per degree of warming in response to rising greenhouse-gas concentrations (Allen & Ingram, 2002; Held & Soden, 2006; Vecchi & Soden, 2007; Jeevanjee & Romps, 2018). This relationship, often referred to as Earth's global hydrological sensitivity, has been found to be remarkably similar across a variety of greenhouse-gas forcing experiments (Stephens & Ellis, 2008; Lambert & Webb, 2008; Andrews & Forster, 2010; Andrews et al., 2010; O'Gorman et al., 2012; Pendergrass & Hartmann, 2014; DeAngelis et al., 2015; Fläschner et al., 2016; Raiter et al., 2023). This implies that global-mean precipitation in past climates, such as the early Eocene or the mid-Pliocene, can be inferred directly from paleoclimate temperature records. For example, it is estimated that early Eocene surface temperatures were 12–15 K warmer than the present-day climate (Caballero & Huber, 2013; Anagnostou et al., 2016; Inglis et al., 2020), which suggests that global-mean precipitation would have been 12–45 % larger than today.

While the global hydrological sensitivity is a conceptually convenient metric, there is evidence that it varies as a function of climate state, implying that estimates from climates similar to today may not apply to past climates. For instance, O'Gorman and Schneider (2008) simulated a wide range of climates in an idealized GCM and showed that global-mean precipitation ceases to increase with warming in hot climates. Examination of the surface energy budget showed that in hot climates, global-mean precipitation is entirely balanced by absorbed shortwave radiation at the surface, which in the idealized GCM, is insensitive to warming (O'Gorman & Schneider, 2008). However, the idealized GCM simulations employed a simple gray radiation scheme and contained no land, sea ice, or clouds, leaving questions about the behavior of precipitation in comprehensive GCMs.

More recent work examined precipitation in comprehensive GCMs under various atmospheric carbon dioxide (CO_2) levels and found that the global hydrological sensitivity exhibits weak climate state dependence. Good et al. (2012) used a coupled GCM and found that global-mean precipitation is only slightly less sensitive to warming in warm climates. Raiter et al. (2023) examined a broader suite of coupled GCMs and found that the global hydrological sensitivity changes little under large CO_2 forcing. However, these studies did not explore extremely high atmospheric CO_2 concentrations and only simulated a narrow range of Cenozoic Era surface temperatures. Thus, in comprehensive GCMs, it remains unclear whether the global hydrological sensitivity is weaker in hot climates and whether precipitation exhibits significant climate state dependence. Notably, analytical radiative arguments introduced by Jeevanjee and Romps (2018) suggest that in hot climates, precipitation may decrease under warming. Yet, this hypothesis has not been confirmed in comprehensive GCMs, which contain clouds and other processes that can modulate radiative fluxes.

In this study, we examine precipitation over a wide range of climates simulated with comprehensive GCMs. We find that in the Community Atmosphere Model (CAM), global-mean precipitation increases approximately linearly with global-mean surface temperatures up to about 330 K, where it peaks at a rate of approximately 5 mm day^{-1}. Beyond 330 K, global-mean precipitation decreases substantially despite increasing global-mean surface temperatures. The decrease in precipitation occurs because in hot climates, Earth's atmosphere contains more water vapor, resulting in increased absorption of shortwave radiation within the atmosphere and decreased absorption of shortwave radiation at the surface, thereby limiting the energy available for surface evaporation. Other GCMs indicate global-mean precipitation might exhibit a smaller maximum rate and begin to decrease at lower surface temperatures. We also find that extratropical precipitation continues to increase despite decreasing global-mean precipitation because of increased poleward latent energy transport. These results have large implications for understanding Earth's hydrological cycle across various epochs, spanning from the recent past to the Hadean and Archaean eons, as well as for understanding weathering in past climates, and the habitability of other Earth-like planets.

2 Data and methods

2.1 Climate model output

We use simulation output from a suite of comprehensive GCMs that have participated in different phases of the Coupled Model Intercomparison Project. The simulations come from different GCMs and span a wide range of surface temperatures, enabling us to explore the impact of model physics on precipitation as a function of climate state.

2.1.1 Community Atmosphere Model (CAM)

We use a suite of simulations from CAM4, CAM5, and CAM6, which are state-of-the-art atmospheric models within the Community Earth System Model (CESM; Hurrell et al., 2013; Danabasoglu et al., 2020). CAM4 uses different radiative transfer code (Collins et al., 2006) from CAM5 and CAM6, which both use the rapid radiative transfer model for GCMs (Mlawer et al., 1997). CAM4, CAM5, and CAM6 also differ substantially in their physical parameterizations of convection and clouds, leading to different equilibrium climate sensitivities of 3.1 K, 4.2 K, and 5.3 K, respectively (Zhu & Poulsen, 2020).

Each CAM simulation is performed with a slab-ocean model (SOM) and specified atmospheric CO_2 concentration. The framework is described in more detail by Zhu and Poulsen (2020). In short, CAM6 simulations were carried out with 1×, 2×, and 4× the preindusitrial CO_2 concentration (284.7 ppmv); CAM5 simulations were carried out with 1×, 2×, 4×, and 8× CO_2; and CAM4 simulations were carried out with 1×, 2×, 4×, 8×, 16×, 32× and 64× CO_2. With CAM4, we perform two additional simulations (128× and 256× CO_2) not described by Zhu and Poulsen (2020). Note that model instability for CAM6 with 8×CO_2 and CAM5 with 16×CO_2 prevented higher CO_2 simulations. Each set of SOM simulations employ identical non-CO_2 preindustrial boundary conditions and mixed layer depths and heat transport convergence derived from corresponding fully coupled preindustrial simulations with a dynamical ocean. All CAM4 and CAM5 simulations were run with a horizontal resolution of 1.9° × 2.5° (latitude × longitude) for 60 model years, except for the CAM4 64×, 128×, and 256×CO_2 simulations, which were run for 80 model years. All CAM6 simulations were run for 80 model years. The last 20 years of each simulation were used to calculate climatologies. The global-mean surface temperature range covered by these simulations is broadly comparable to paleoclimate temperatures over the Cenozoic Era and beyond.

We also use a suite of climate simulations that are described in more detail by Wolf et al. (2018). These simulations use a modified version of CAM4 with a SOM and a horizontal resolution of 4° × 5°. The modified version of CAM4 uses a correlated-k radiative transfer model to accurately simulate extremely warm climates (Wolf & Toon, 2013). We use 22 simulations with atmospheric CO_2 concentrations starting from 1.40625 ppmv and doubling until 2,949,120 ppmv.

2.1.2 LongRunMIP

We use a set of simulations from LongRunMIP (Rugenstein et al., 2019), which is a model intercomparison project that aims to better understand centennial and millennial time scale atmosphere–ocean processes in comprehensive, coupled GCMs. We use all GCMs that provide a preindustrial control simulation and 2×, 4×, 8×, and 16× CO_2. There are no simulations with higher CO_2 forcing. We assume that each preindustrial control simulation has an atmospheric CO_2 concentration of 284.7 ppmv. For all simulations, except those from CNRM-CM6-1, we average each variable over years 970–1,000. For the CNRM-CM6-1 simulations, we average over years 720–750 as this is the longest available time period after 2×CO_2. Most simulations have little-to-no global-mean ocean heat uptake and are therefore close to equilibrium at this time period.

2.2 Energy budget diagnostics

2.2.1 Global

Global-mean precipitation can be examined through the surface energy budget. The global-mean (denoted by an overbar) surface energy budget can be expressed as

$$0 = \bar{S} - \bar{L} - L_v\bar{E} - \bar{H} - \bar{G}, \tag{1}$$

where S is the net downward shortwave flux, L is the net upward longwave flux, E is the surface evaporation flux, L_v is the latent heat of vaporization, H is the sensible heat flux from the surface into the atmosphere, and G is ocean heat uptake and storage. On interannual and longer timescales, $\bar{E}$ is equal to precipitation $\bar{P}$, which results in

$$\bar{P} \equiv \bar{E} = \frac{1}{L_v}\left(\bar{S} - \bar{L} - \bar{H} - \bar{G}\right). \tag{2}$$

The radiative fluxes S and L can be further decomposed into clear-sky (clr) and cloud components (cld) such that $S = S_{\text{clr}} + S_{\text{cld}}$ and $L = L_{\text{clr}} + L_{\text{cld}}$. For the CAM simulations, we decompose S and L into clear-sky and cloud components, while for the LongRunMIP simulations, we cannot decompose S and L due to the lack of clear-sky surface flux output.

O'Gorman and Schneider (2008) showed that Eq. (2) can explain the structure of global-mean precipitation as a function of climate state, including the processes controlling the maximum rate of precipitation in hot climates.

2.2.2 Regional

Regional precipitation can also be examined through the surface energy budget with the addition of the latent energy flux divergence $\nabla \cdot F_{\text{latent}}$. On long time scales,

$$P - E = -\frac{1}{L_v}\nabla \cdot F_{\text{latent}}, \tag{3}$$

which means that, using the surface energy budget, regional precipitation can be expressed as

$$P = \frac{1}{L_v}\left(S - L - H - G - \nabla \cdot F_{\text{latent}}\right). \tag{4}$$

We examine regional precipitation through the surface energy budget as it connects directly to our approach for global-mean precipitation and provides a physically intuitive understanding of energetic constraints on evaporation, which is how moisture enters the atmosphere. Note that integrating Eq. (4) globally results in exactly Eq. (2). Global and regional precipitation can also be examined through the atmospheric energy budget (e.g., Muller & O'Gorman, 2011; O'Gorman et al., 2012; Pendergrass & Hartmann, 2014; Bonan, Feldl, et al., 2023).

3 Precipitation over a wide range of climates

3.1 Global-mean precipitation

We begin by examining global-mean precipitation as a function of atmospheric CO_2 concentration and global-mean surface temperature (Fig. 1). Under high CO_2 concentrations, GCMs exhibit large intermodel differences in global-mean surface temperatures (Fig. 1a). For example, across GCMs, global-mean surface temperatures for CO_2 concentrations near 1,000 ppmv range from 289 K to 300 K. While the intermodel spread in surface temperatures is large, these simulations, with the exception of CAM4 (blue and red lines, Fig. 1a), only span a small range of Cenezoic Era paleoclimate temperatures. The two versions of CAM4 with different radiation schemes simulate an even larger range of global-mean surface temperatures, ranging from 265 K to 380 K (blue and red lines, Fig. 1a). Note these simulations indicate that Earth's climate sensitivity exhibits considerable state dependence for global-mean surface temperatures around 310 K, which has been noted in several other studies (e.g., Caballero & Huber, 2013; Wolf et al., 2018; Zhu & Poulsen, 2020; Seeley & Jeevanjee, 2021; Henry et al., 2023).

GCMs also exhibit a large intermodel spread in global-mean precipitation as a function of atmospheric CO_2 concentration (Fig. 1b). For example, across GCMs, global-mean precipitation for CO_2 concentrations near 1,000 ppmv ranges from approximately 2.8 mm day^{-1} to approximately 4.0 mm day^{-1}. Interestingly, for CO_2 concentrations beyond 30,000 ppmv, the CAM4 simulations indicate that global-mean precipitation decreases (Fig. 1b) despite surface temperature increases (Fig. 1a). Both versions of CAM4 exhibit a global-mean precipitation decrease, despite having different radiation codes (blue and red lines, Fig. 1b).

These results can be further understood by plotting global-mean precipitation as a function of global-mean surface temperature; the derivative of this function is the global hydrological sensitivity (Fig. 1c). From cold ($\sim$ 270 K) to warm ($\sim$ 320 K) climates, global-mean precipitation exhibits a fairly linear relationship with global-mean surface temperature, with only slight decreases in the rate of global-mean precipitation increase. In hot ($>$ 320 K) climates, the CAM4 simulations indicate that global-mean precipitation increases more slowly with global-mean surface temperature and eventually decreases at approximately 330 K (Fig. 1c). In the CAM4 simulation with the more accurate radiation code, global-mean precipitation continues to decrease substantially despite increasing surface temperatures. Note that other GCMs, such as MPI-ESM1.2 and HadCM3L, exhibit overall weaker increases in precipitation for the same surface temperature range as the CAM simulations (gold and light blue lines, Fig. 1c).

To understand the mechanisms contributing to global-mean precipitation as a function of global-mean surface temperature, we examine the surface energy budget (see Section 2.2.1). Figure 2 shows the components of the surface energy budget (converted from W m^{-2} to mm day^{-1}). The clear-sky and cloud components of the net surface shortwave and net surface longwave fluxes are shown in Figure S1.

From cold to warm climates, the global-mean net surface shortwave flux exhibits relatively little change, though there is large intermodel spread (Fig. 2a). For example, the CAM simulations exhibit little change in the net surface shortwave flux, whereas MPI-ESM1.2 exhibits a strong decrease. From cold to warm climates, both the net surface longwave flux and surface sensible heat flux approach zero with little intermodel spread (Fig. 2b and 2c). The net surface longwave flux change is almost entirely driven by the clear-sky component (Fig. S1).

In hot climates, the net surface longwave flux and surface sensible heat flux are zero or slightly positive (Fig. 2b, 2c). This occurs because differences in surface and tropospheric air temperatures become small, and the atmosphere approaches the optically thick limit, where upward longwave emission at the surface and the downward longwave emission from within the atmosphere that reaches the surface occur at almost the same temperature (O'Gorman & Schneider, 2008). As a result, global-mean evaporation, and thus global-mean precipitation, is almost entirely balanced by the net surface shortwave flux, which exhibits a strong decrease in hot climates (Fig. 2a). The clear-sky component of the net surface shortwave flux decreases in hot climates (Fig. S1) because of increased shortwave absorption by the atmosphere due to water vapor (Fig. S2). The decrease in net surface shortwave flux occurs in both CAM4 simulations, though the decrease is stronger at high temperatures in the CAM4 simulations with the more accurate radiation code (blue and red lines, Fig. 2a).

3.2 Zonal-mean precipitation

We now examine zonal-mean precipitation as a function of global-mean surface temperature (Fig. 3). We focus on the CAM simulations to understand the regions contributing to the decrease in global-mean precipitation for surface temperatures beyond 330 K. The same analysis for each simulation from LongRunMIP is shown in Figure S3.

From cold to warm climates, precipitation increases in most regions, with substantial increases in the tropics and extratropics and small decreases in the subtropics (Fig. 3a). In hot climates (> 320 K), subtropical and tropical precipitation decreases substantially. The maximum tropical precipitation is approximately 10 mm day^{-1} in warm climates and decreases to approximately 5 mm day^{-1} in hot climates. Similarly, subtropical precipitation decreases from approximately 6 mm day^{-1} in warm climates to approximately 0 mm day^{-1} in hot climates. Notably, from warm to hot climates, despite a decrease in global-mean precipitation, precipitation continues to increase in the extratropics, with the polar regions experiencing a substantial increase in precipitation (Fig. 3a). Precipitation in the Arctic, for instance, increases from approximately 2 mm day^{-1} in warm climates to approximately 8 mm day^{-1} in hot climates.

To understand the mechanisms contributing to regional precipitation as a function of global-mean surface temperature, we examine components of the surface energy budget and latent energy flux divergence (see Section 2.2.2). Figures 3b-e show the components of the zonal-mean surface energy budget and latent energy flux divergence (converted from W m^{-2} to mm day^{-1}) for the CAM simulations.

From cold to warm climates, the net surface shortwave flux remains relatively constant, exhibiting weak increases in the polar regions (Fig. 3b). Figure S4 shows the clear-sky and cloud components of the zonal-mean net surface shortwave flux and shows that this is related mainly to the clear-sky component. The overall increase in zonal-mean precipitation from cold to warm climates is contributed mainly by the net surface longwave flux, which becomes smaller under warming (Fig. 3c). The surface sensible heat flux contributes weakly to the overall increase in zonal-mean precipitation from cold to warm climates (Fig. 3d). The latent energy flux divergence contributes most to the zonal-mean pattern of precipitation, causing a precipitation increase in the tropics and extratropics, and a precipitation decrease in the subtropics (Fig. 3e). Note there are substantial changes in the latent energy flux divergence around 320 K that indicate meridional shifts in tropical rainfall, expansion of the subtropics, and poleward shifts of the midlatitude stormtracks.

In hot climates (> 320 K), the net surface longwave flux and surface sensible heat flux become much smaller and approach zero (Fig. 3c, 3d). As a result, in hot climates, regional precipitation is almost entirely balanced by the net surface shortwave flux and latent energy flux divergence (Fig. 3b, 3e). In the subtropics, the weak export of moisture associated with increased poleward latent energy transport (Fig. 3e) is balanced almost entirely by the net surface shortwave flux, resulting in no precipitation (Fig. 3a). Note that the subtropics continue to see drying in extremely hot climates, largely due to the increased latent energy transport (Fig. 3e). In the extratropics, precipitation continues to increase in hot climates because of increased poleward latent energy transport. In the polar regions, the decrease in net surface shortwave flux is small (Fig. 3b), but the increase in poleward latent energy transport is large (Fig. 3e), resulting in a overall precipitation increase (Fig. 3a).

3.3 Total precipitable water and precipitation intensity

The decrease in global-mean precipitation for surface temperatures above 330 K has important implications for precipitation intensity and precipitation extremes. Scaling arguments and simulations suggest that precipitation extremes depend primarily on the atmospheric water vapor content (O'Gorman & Schneider, 2009; O'Gorman & Schneider, 2009), which should continue to increase with warming (O'Gorman & Schneider, 2008). A decrease in global-mean precipitation but increase in global-mean atmospheric water vapor content implies that precipitation would have to become more episodic and potentially more intense.

Due to the lack of high-frequency temporal output, we are unable to quantitatively examine precipitation extremes (e.g., O'Gorman & Schneider, 2009; O'Gorman & Schneider, 2009). However, we can examine the total precipitable water and calculate the water vapor residence time, defined as the global-mean total precipitable water divided by the global-mean precipitation (Trenberth, 1998; Bosilovich et al., 2005). The water vapor residence time can help indicate precipitation intensity. For instance, a climate with the same mean precipitation as today but a longer water vapor residence time implies there is more episodic and intense precipitation.

The global-mean total precipitable water (Fig. 4a) and global-mean water vapor residence time (Fig. 4b) increase with increasing global-mean surface temperatures. From cold to warm climates, total precipitable water increases at a rate of 6–7 % K^{-1} and the water vapor residence time increases at a rate of 4–5 % K^{-1}. In hot climates, the total precipitable water continues to increase (Fig. 4a), resulting in a global-mean water vapor residence time of approximately one year at 350 K (Fig. 4b). The total precipitable water increases most in the tropics and subtropics (Fig. 4c), which likely results in regional variations of precipitation intensity. For climates between 320–330 K, precipitation is likely more intense and episodic due to the relatively similar global-mean precipitation (Fig. 1c) but increase in water vapor residence time (Fig. 4b).

4 Discussion and conclusions

In this study, we examined precipitation over a wide range of climates simulated with comprehensive GCMs. Building on earlier work by O'Gorman and Schneider (2008), we showed that global-mean precipitation increases approximately linearly with global-mean surface temperatures from cold to warm climates and begins to increase more slowly in hot climates (Fig. 1c)—consistent with Good et al. (2012). However, in contrast to these studies, we found that global-mean precipitation decreases substantially after 330 K, despite increasing surface temperatures (Fig. 1c). This occurs because global-mean precipitation is almost entirely balanced by the absorbed shortwave radiation at the surface in hot climates (Fig. 2). As the climate warms, Earth's atmosphere contains more water vapor, resulting in increased absorption of shortwave radiation within the atmosphere and decreased absorption of shortwave radiation at the surface (Fig. 2a and Fig. S2). This limits the energy available for surface evaporation and causes a decrease in global-mean precipitation with further warming. The results confirm the analytical radiative arguments of Jeevanjee and Romps (2018) but in comprehensive GCMs with cloud radiative processes.

The decrease in global-mean precipitation for surface temperatures beyond 330 K is driven by a decrease in tropical and subtropical precipitation (Fig. 3a). Extratropical precipitation continues to increase, despite a decrease in global-mean precipitation (Fig. 3a). This occurs because of increases in poleward latent energy transport (Fig. 3e), which is a well-known feature of hot climates (Caballero & Langen, 2005; O'Gorman & Schneider, 2008). However, the increase in poleward latent energy transport exhibits significant deviations from the increase expected solely from the Clausius-Clapeyron relation (Held & Soden, 2006). These deviations include meridional shifts in tropical rainfall, expansions and contractions of the subtropical regions, and poleward migrations of the extratropical storm tracks. A series of studies have shown that a one-dimensional moist energy balance model can accurately simulate poleward moisture transport in comprehensive GCMs (Siler et al., 2018; Armour et al., 2019; Bonan, Siler, et al., 2023; Bonan et al., 2024), suggesting that downgradient energy transport might explain the range of poleward latent transport seen in CAM4, including dynamical changes associated with the Hadley circulations.

While our results show considerable climate state dependence in precipitation, the simulations used are driven purely by changes in atmospheric CO_2 concentrations and do not contain changes in other boundary conditions that impact hot climates (see review by Zhu et al., 2024). For example, the early Eocene experienced significant changes in orbital dynamics (Lourens et al., 2005) as well as in continental land configurations and ocean circulation (Barron, 1987; Shellito et al., 2009; Green & Huber, 2013), each of which could potentially alter the surface energy budget. Examining the effect of other forcings on precipitation in hot climates might change these results.

Despite this caveat, our work has implications for other aspects of Earth's hydrological cycle. We showed that global-mean total precipitable water increases more strongly with warming when compared to global-mean precipitation (Fig. 4a and Fig. 1c), which results in a longer global-mean water vapor residence time (Fig. 4b). Thus, precipitation would have to become more episodic at high surface temperatures. However, due to the lack of higher-frequency output we are unable to quantitatively examine precipitation intensity and precipitation extremes. Note that recent work showed precipitation in hot climates is indeed more episodic and occurs in short and intense outbursts separated by multi-day dry spells (Seeley & Wordsworth, 2021; Dagan et al., 2023). However, these studies employed an idealized cloud-resolving model with limited domains. It remains unclear what episodic precipitation looks like in hot climates simulated with comprehensive GCMs. Future work should explore other characteristics of precipitation in hot climates. Such work will help to better understand mechanisms for hydrological change in past and future climates.

Overall, our results show that precipitation is strongly dependent on the climate state. While the CAM simulations indicate that global-mean precipitation exhibits a maximum rate of approximately 5 mm day^{-1} and decreasing rates for surface temperatures beyond 330 K, other GCMs, like HadCM3L and MPI-ESM1.2, indicate that global-mean precipitation might exhibit a smaller maximum rate and begin to decrease at lower surface temperatures. These differences are attributable to shortwave radiation and may be related to water vapor absorption parameterizations in comprehensive GCMs (e.g., Yang et al., 2016). Hence, there is a need to examine Earth's hydrological cycle in hot climates simulated with a broader suite of comprehensive GCMs. Such work will have large implications for understanding various climate epochs, spanning from the recent past to the Hadean and Archaean eons, as well as for understanding weathering in past climates, and the habitability of other Earth-like planets.

Acknowledgments

The authors thank Thorsten Mauritsen for helpful comments during early stages of this research. D.B.B was supported the National Science Foundation (NSF) Graduate Research Fellowship Program (NSF Grant DGE1745301). This material is based upon work supported by the National Center for Atmospheric Research (NCAR), which is a major facility sponsored by the NSF under Cooperative Agreement 1852977.

Data Availability Statement

CAM4, CAM5, and CAM6 output is available in the Zenodo repository (`https://doi.org/10.5281/zenodo.3695929`). LongRunMIP output is freely available at `http://www.longrunmip.org/`. The CAM4 output with modified radiation is available at: `https://archive.org/download/EvaluatingClimateSensitivityToCO2AcrossEarthsHistory_201809`

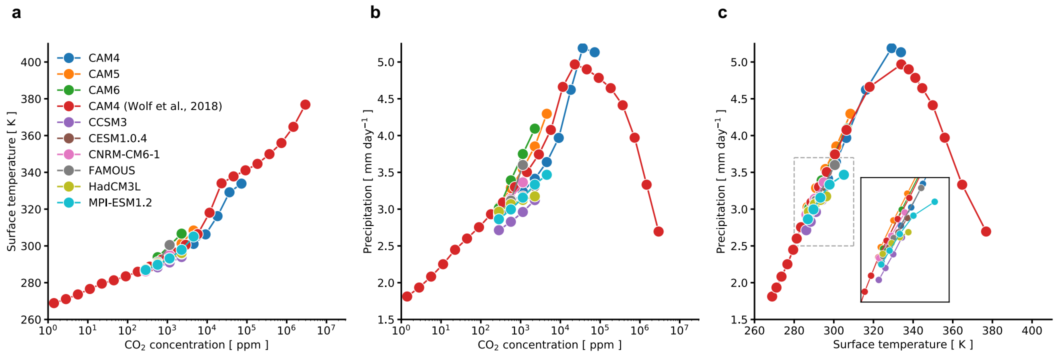

Figure 1. Global-mean precipitation over a wide range of climates. (a) Global-mean surface temperature (K) as a function of the atmospheric CO_2 concentration for the CAM slab-ocean model simulations and fully-coupled LongRunMIP simulations. (b) Same as in (a) but for global-mean precipitation (mm day^{-1}). (c) Same as in (b) but for global-mean precipitation as a function of global-mean surface temperature. The inset in (c) shows an enlarged version of the grey dashed box.

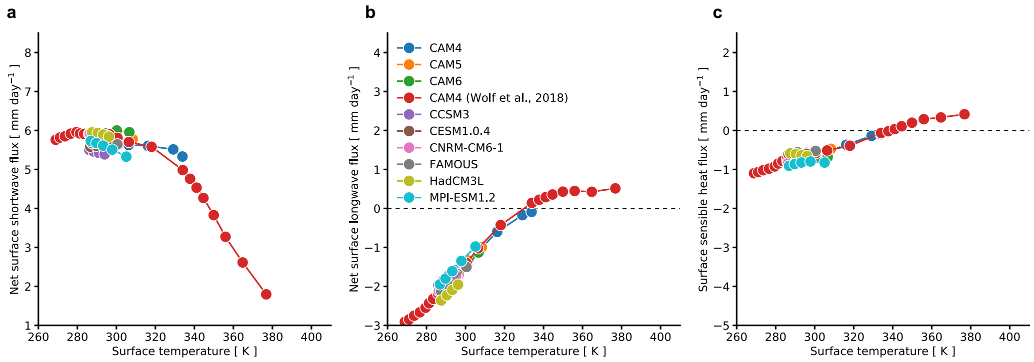

Figure 2. Contributions to global-mean precipitation over a wide range of climates. The global-mean (a) net surface shortwave flux, (b) net surface longwave flux, and (c) surface sensible heat flux as a function of global-mean surface temperature for the CAM slab-ocean model simulations and fully-coupled LongRunMIP simulations. Ocean heat uptake is near-zero for all simulations and is not shown.

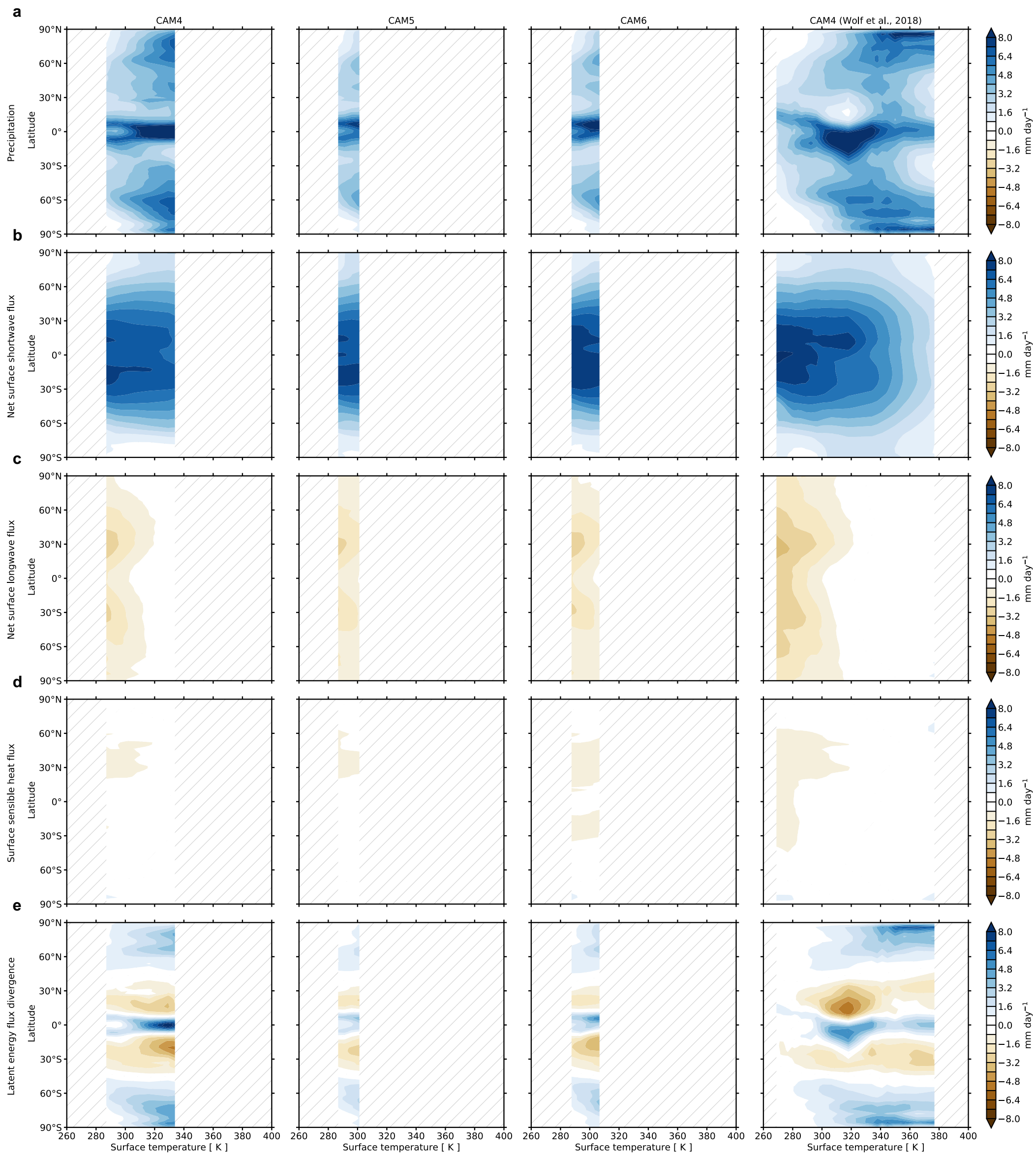

Figure 3. Zonal-mean precipitation over a wide range of climates. (a) The zonal-mean precipitation as a function of global-mean surface temperature for the CAM4, CAM5, and CAM6 simulations. The zonal-mean (b) net surface shortwave flux, (c) net surface longwave flux, (d) surface sensible heat flux, and (e) latent energy flux divergence (converted from W m^{-2} to mm day^{-1}) as a function of global-mean surface temperature for the CAM4, CAM5, and CAM6 simulations. Ocean heat uptake is zero for all simulations and is not shown. Panels (b-e) add to panel (a). The light grey hatching indicates no simulation data.

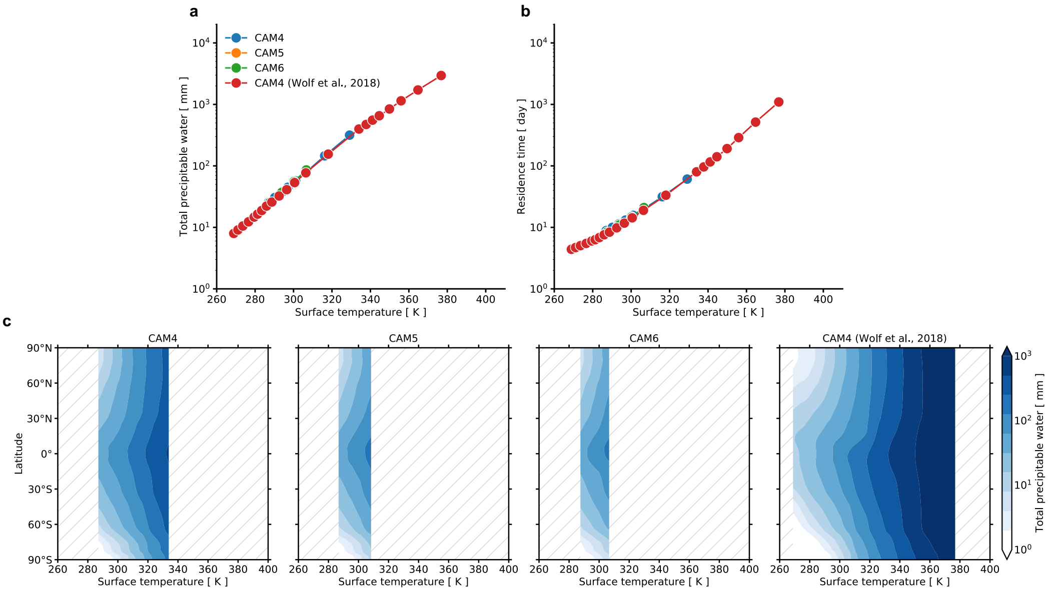

Figure 4. Residence time of water vapor over a wide range of climates. The global-mean (a) total precipitable water and (b) residence time of water vapor. The (blue) CAM4, (orange) CAM5, and (green) CAM6 simulations use a slab-ocean model with the Rapid Radiative Transfer Model and the (red) CAM4 simulation uses a slab-ocean model with a more accurate radiation model for high temperatures. (c) Zonal-mean total precipitable water as a function of global-mean surface temperature for the CAM4, CAM5, and CAM6 simulations. The light grey hatching indicates no simulation data.

References

Allen, M. R., & Ingram, W. J. (2002). Constraints on future changes in climate and the hydrologic cycle. *Nature*, *419*(6903), 224–232.

Anagnostou, E., John, E. H., Edgar, K. M., Foster, G. L., Ridgwell, A., Inglis, G. N., ... Pearson, P. N. (2016). Changing atmospheric CO2 concentration was the primary driver of early Cenozoic climate. *Nature*, *533*(7603), 380–384.

Andrews, T., & Forster, P. M. (2010). The transient response of global-mean precipitation to increasing carbon dioxide levels. *Environmental Research Letters*, *5*(2), 025212.

Andrews, T., Forster, P. M., Boucher, O., Bellouin, N., & Jones, A. (2010). Precipitation, radiative forcing and global temperature change. *Geophysical research letters*, *37*(14).

Armour, K. C., Siler, N., Donohoe, A., & Roe, G. H. (2019). Meridional atmospheric heat transport constrained by energetics and mediated by large-scale diffusion. *Journal of Climate*, *32*(12), 3655–3680.

Barron, E. J. (1987). Eocene equator-to-pole surface ocean temperatures: A significant climate problem? *Paleoceanography*, *2*(6), 729–739.

Bonan, D. B., Feldl, N., Siler, N., Kay, J. E., Armour, K. C., Eisenman, I., & Roe, G. H. (2024). The influence of climate feedbacks on regional hydrological changes under global warming. *Geophysical Research Letters*, *51*(3), e2023GL106648.

Bonan, D. B., Feldl, N., Zelinka, M. D., & Hahn, L. C. (2023). Contributions to regional precipitation change and its polar-amplified pattern under warming. *Environmental Research: Climate*, *2*(3), 035010.

Bonan, D. B., Siler, N., Roe, G. H., & Armour, K. C. (2023). Energetic constraints on the pattern of changes to the hydrological cycle under global warming. *Journal of Climate*, *36*(10), 3499–3522.

Bosilovich, M. G., Schubert, S. D., & Walker, G. K. (2005). Global changes of the water cycle intensity. *Journal of Climate*, *18*(10), 1591–1608.

Caballero, R., & Huber, M. (2013). State-dependent climate sensitivity in past warm climates and its implications for future climate projections. *Proceedings of the National Academy of Sciences*, *110*(35), 14162–14167.

Caballero, R., & Langen, P. L. (2005). The dynamic range of poleward energy transport in an atmospheric general circulation model. *Geophysical Research Letters*, *32*(2).

Collins, W. D., Bitz, C. M., Blackmon, M. L., Bonan, G. B., Bretherton, C. S., Carton, J. A., ... others (2006). The community climate system model version 3 (CCSM3). *Journal of Climate*, *19*(11), 2122–2143.

Dagan, G., Seeley, J. T., & Steiger, N. (2023). Convection and Convective-Organization in Hothouse Climates. *Journal of Advances in Modeling Earth Systems*, *15*(11), e2023MS003765.

Danabasoglu, G., Lamarque, J.-F., Bacmeister, J., Bailey, D., DuVivier, A., Edwards, J., ... others (2020). The community earth system model version 2 (CESM2). *Journal of Advances in Modeling Earth Systems*, *12*(2), e2019MS001916.

DeAngelis, A. M., Qu, X., Zelinka, M. D., & Hall, A. (2015). An observational radiative constraint on hydrologic cycle intensification. *Nature*, *528*(7581), 249–253.

Fläschner, D., Mauritsen, T., & Stevens, B. (2016). Understanding the intermodel spread in global-mean hydrological sensitivity. *Journal of Climate*, *29*(2), 801–817.

Good, P., Ingram, W., Lambert, F. H., Lowe, J. A., Gregory, J. M., Webb, M. J., ... Wu, P. (2012). A step-response approach for predicting and understanding non-linear precipitation changes. *Climate Dynamics*, *39*, 2789–2803.

Green, J., & Huber, M. (2013). Tidal dissipation in the early Eocene and implications for ocean mixing. *Geophysical Research Letters*, *40*(11), 2707–2713.

Held, I. M., & Soden, B. J. (2006). Robust responses of the hydrological cycle to global warming. *Journal of climate*, *19*(21), 5686–5699.

Henry, M., Vallis, G. K., Lutsko, N. J., Seeley, J. T., & McKim, B. A. (2023). State-Dependence of the Equilibrium Climate Sensitivity in a Clear-Sky GCM. *Geophysical Research Letters*, *50*(23), e2023GL104413.

Hurrell, J. W., Holland, M. M., Gent, P. R., Ghan, S., Kay, J. E., Kushner, P. J., ... others (2013). The community earth system model: a framework for collaborative research. *Bulletin of the American Meteorological Society*, *94*(9), 1339–1360.

Inglis, G. N., Bragg, F., Burls, N., Evans, D., Foster, G. L., Huber, M., ... others (2020). Global mean surface temperature and climate sensitivity of the EECO, PETM and latest Paleocene. *Climate of the past Discussions*, *2020*, 1–43.

Jeevanjee, N., & Romps, D. M. (2018). Mean precipitation change from a deepening troposphere. *Proceedings of the National Academy of Sciences*, *115*(45), 11465–11470.

Lambert, F. H., & Webb, M. J. (2008). Dependency of global mean precipitation on surface temperature. *Geophysical Research Letters*, *35*(16).

Lourens, L. J., Sluijs, A., Kroon, D., Zachos, J. C., Thomas, E., Röhl, U., ... Raffi, I. (2005). Astronomical pacing of late Palaeocene to early Eocene global warming events. *Nature*, *435*(7045), 1083–1087.

Mlawer, E. J., Taubman, S. J., Brown, P. D., Iacono, M. J., & Clough, S. A. (1997). Radiative transfer for inhomogeneous atmospheres: RRTM, a validated correlated-k model for the longwave. *Journal of Geophysical Research: Atmospheres*, *102*(D14), 16663–16682.

Muller, C. J., & O'Gorman, P. (2011). An energetic perspective on the regional response of precipitation to climate change. *Nature Climate Change*, *1*(5), 266–271.

O'Gorman, P. A., & Schneider, T. (2009). The physical basis for increases in precipitation extremes in simulations of 21st-century climate change. *Proceedings of the National Academy of Sciences*, *106*(35), 14773–14777.

O'Gorman, P. A., Allan, R. P., Byrne, M. P., & Previdi, M. (2012). Energetic constraints on precipitation under climate change. *Surveys in geophysics*, *33*, 585–608.

O'Gorman, P. A., & Schneider, T. (2008). The hydrological cycle over a wide range of climates simulated with an idealized GCM. *Journal of Climate*, *21*(15), 3815–3832.

O'Gorman, P. A., & Schneider, T. (2009). Scaling of precipitation extremes over a wide range of climates simulated with an idealized GCM. *Journal of Climate*, *22*(21), 5676–5685.

Pendergrass, A. G., & Hartmann, D. L. (2014). The atmospheric energy constraint on global-mean precipitation change. *Journal of climate*, *27*(2), 757–768.

Raiter, D., Polvani, L. M., Mitevski, I., Pendergrass, A. G., & Orbe, C. (2023). Little change in apparent hydrological sensitivity at large CO2 forcing. *Geophysical Research Letters*, *50*(18), e2023GL104954.

Rugenstein, M., Bloch-Johnson, J., Abe-Ouchi, A., Andrews, T., Beyerle, U., Cao, L., ... others (2019). LongRunMIP: motivation and design for a large collection of millennial-length AOGCM simulations. *Bulletin of the American Meteorological Society*, *100*(12), 2551–2570.

Seeley, J. T., & Jeevanjee, N. (2021). H2O windows and CO2 radiator fins: A clear-sky explanation for the peak in equilibrium climate sensitivity. *Geophysical Research Letters*, *48*(4), e2020GL089609.

Seeley, J. T., & Wordsworth, R. D. (2021). Episodic deluges in simulated hothouse climates. *Nature*, *599*(7883), 74–79.

Shellito, C. J., Lamarque, J.-F., & Sloan, L. C. (2009). Early Eocene Arctic climate sensitivity to pCO2 and basin geography. *Geophysical Research Letters*, *36*(9).

Siler, N., Roe, G. H., & Armour, K. C. (2018). Insights into the zonal-mean response of the hydrologic cycle to global warming from a diffusive energy balance model. *Journal of Climate*, *31*(18), 7481–7493.

Stephens, G. L., & Ellis, T. D. (2008). Controls of global-mean precipitation increases in global warming GCM experiments. *Journal of Climate*, *21*(23), 6141–6155.

Trenberth, K. E. (1998). Atmospheric moisture residence times and cycling: Implications for rainfall rates and climate change. *Climatic change*, *39*, 667–694.

Vecchi, G. A., & Soden, B. J. (2007). Global warming and the weakening of the tropical circulation. *Journal of Climate*, *20*(17), 4316–4340.

Wolf, E., Haqq-Misra, J., & Toon, O. (2018). Evaluating climate sensitivity to CO2 across Earth's history. *Journal of Geophysical Research: Atmospheres*, *123*(21), 11–861.

Wolf, E., & Toon, O. (2013). Hospitable Archean climates simulated by a general circulation model. *Astrobiology*, *13*(7), 656–673.

Yang, J., Leconte, J., Wolf, E. T., Goldblatt, C., Feldl, N., Merlis, T., ... others (2016). Differences in water vapor radiative transfer among 1D models can significantly affect the inner edge of the habitable zone. *The Astrophysical Journal*, *826*(2), 222.

Zhu, J., & Poulsen, C. J. (2020). On the increase of climate sensitivity and cloud feedback with warming in the community atmosphere models. *Geophysical Research Letters*, *47*(18), e2020GL089143.

Zhu, J., Poulsen, C. J., & Otto-Bliesner, B. L. (2024). Modeling Past Hothouse Climates as a Means for Assessing Earth System Models and Improving the Understanding of Warm Climates. *Annual Review of Earth and Planetary Sciences*, *52*.

Supporting Information:
Precipitation over a wide range of climates simulated with comprehensive GCMs

David B. Bonan[1], Tapio Schneider[1], Jiang Zhu[2]

[1]Environmental Science and Engineering,California Institute of Technology, Pasadena, California, USA
[2]Climate and Global Dynamics, NSF National Center for Atmospheric Research, Boulder, Colorado, USA

April 19, 2024

Table of Contents

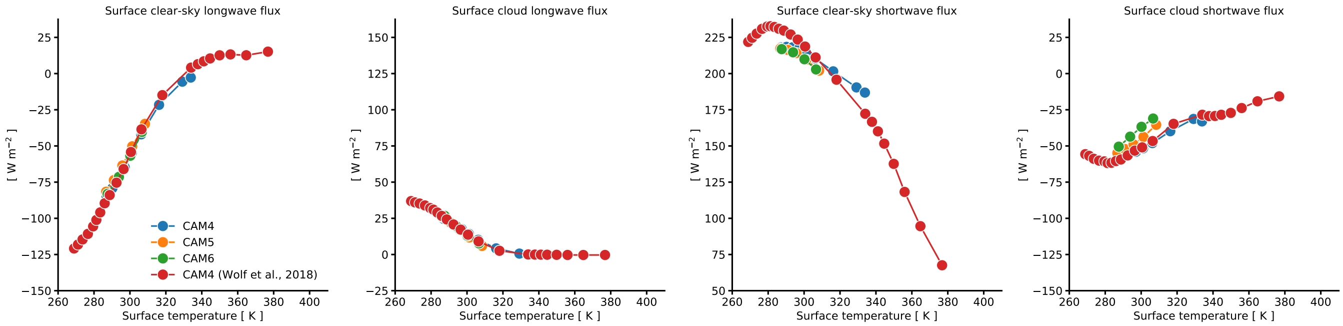

Supplemental Figure 1: **Net surface clear-sky and cloud surface shortwave and longwave fluxes.** Global-mean net surface longwave and shortwave fluxes decomposed into clear-sky and cloud components as a function of global-mean surface temperature for the CAM simulations.

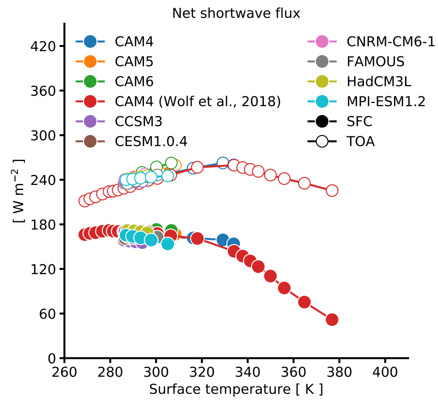

Supplemental Figure 2: **Net top-of-atmosphere and surface shortwave fluxes.** Global-mean net top-of-atmosphere (open circles) and net surface (colored circles) shortwave fluxes as a function of global-mean surface temperature for the CAM and LongRunMIP simulations.

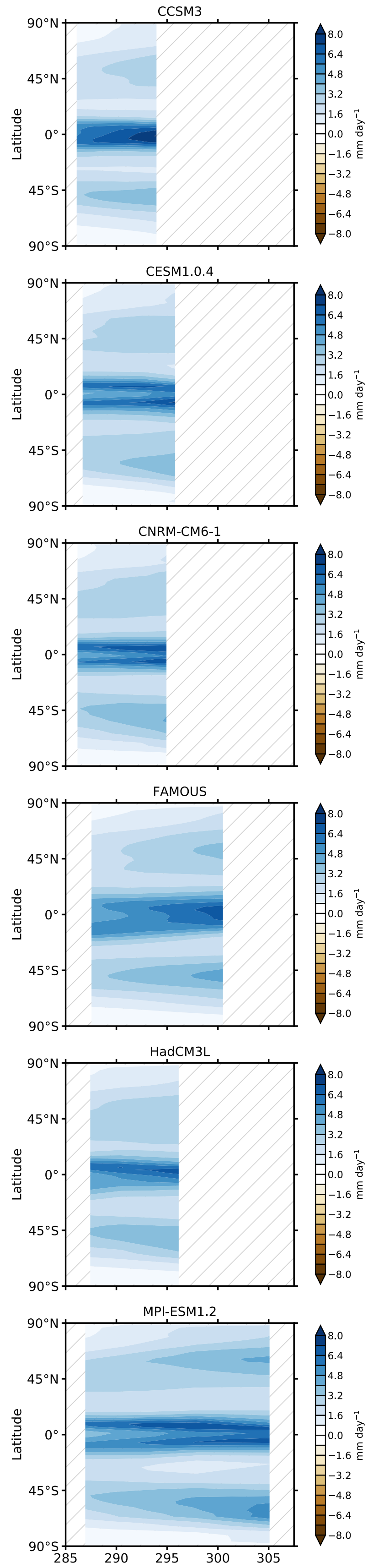

Supplemental Figure 3: **Zonal-mean precipitation as a function of climate state.** Zonal-mean precipitation as a function of global-mean surface temperature for the LongRunMIP simulations. The light grey hatching indicates no simulation data.

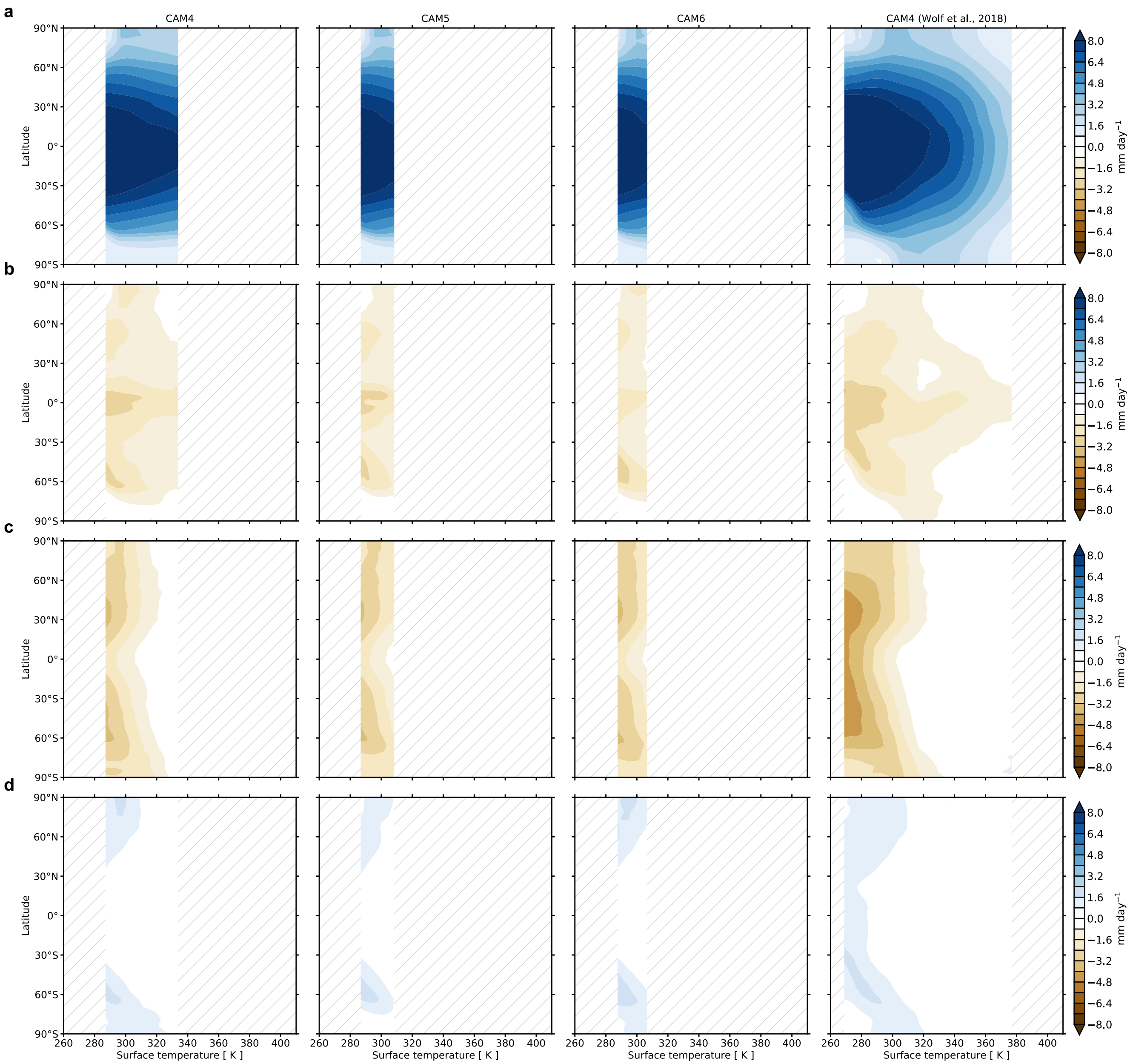

Supplemental Figure 4: **Zonal-mean clear-sky and cloud components of the surface radiative fluxes.** The zonal-mean (a) net surface clear-sky shortwave flux, (b) net surface cloud shortwave flux, (c) net surface clear-sky longwave flux, and (d) net surface cloud longwave flux (converted from W m^{-2} to mm day^{-1}) as a function of global-mean surface temperature for the CAM simulations. The light grey hatching indicates no simulation data.